Crustal structure along the Wanzai–Yongchun profile in the Cathaysia Block, Southeast China, constrained by a joint active- and passive-source seismic experiment

Minfu Huang,[1,2] Tao Xu,[1,3] Qingtian Lü,[4] Jiyan Lin,[1,2,5] Zhiming Bai,[1,3] Yangfan Deng,[6] Yongqian Zhang[4] and José Badal[7]

[1]*State Key Laboratory of Lithospheric Evolution, Institute of Geology and Geophysics, Chinese Academy of Sciences, Beijing* 100029, *China. E-mail:* xutao@mail.iggcas.ac.cn

[2]*University of Chinese Academy of Sciences, Beijing* 100049, *China*

[3]*Innovation Academy for Earth Science, CAS, Beijing* 100029, *China*

[4]*Chinese Academy of Geological Sciences, Beijing* 100037, *China. E-mail:* lqt@cags.ac.cn

[5]*Geophysical Exploration Center, China Earthquake Administration, Zhengzhou* 450002, *China*

[6]*State Key Laboratory of Isotope Geochemistry, Guangzhou Institute of Geochemistry, Chinese Academy of Sciences, Guangzhou* 510640, *China*

[7]*Physics of the Earth, University of Zaragoza, Pedro Cerbuna* 12, *Zaragoza* 50009, *Spain*

SUMMARY

Since the Mesozoic, the South China Block (SCB) has experienced multiple episodes of tectonic magmatism accompanied by metallogenesis. To explore the seismic velocity structure of the crust and its connection with mineralization, we constructed a wide-angle reflection and refraction (WARR) profile by deploying 435 short-period seismometers across the Cathaysia Block in Southeast China. Receiver functions and the H–κ stacking method were applied using a reference 2-D velocity model obtained from the analysis of WARR data. Integration of active- and passive-source seismic data enabled us to obtain an image of the crust and the average Vp/Vs ratio value of the SCB and produce several results: (1) The crustal thickness varies west-to-east from 28 km below the Qinhang metallogenic belt to 32 km below the Wuyishan metallogenic belt, and the average value of the Vp/Vs ratio for the crust is 1.71. Both the thickness of the crust and the average Vp/Vs ratio are lower than the average global values for the continental crust. (2) The relatively low Vp/Vs ratio and thin crust along the profile could be generated by thinning of the lower crust in the SCB as a result of the backarc extension related to westward subduction of the Paleo-Pacific plate below East Asia. (3) The Moho depth estimated from H–κ stacking with the help of the background P-wave velocity model modified by the WARR model fits better than using a global seismic velocity model with its common conversion point image, which supports a potential seismic data analysis technique provided with a joint deployment of both active- and passive-source seismic observation system with a shorter period.

Key words: Joint inversion; Image processing; Crustal imaging; Crustal structure; Asia.

1 INTRODUCTION

Wide-angle reflection and refraction (WARR) allows us to use ground motion data to produce fine-scale velocity models (Zhang & Wang 2007; Zhang *et al.* 2013b; Kuo *et al.* 2016; Lin *et al.* 2021). However, this method generally requires some restrictions on velocity interfaces such as the Moho. Broad-band seismometers are widely used in passive-source seismic observations in lithospheric-scale geophysical studies that are able to provide independent estimates of these interfaces (Zhou *et al.* 2012; He *et al.* 2013, 2014;

Bao *et al.* 2015; Zhang *et al.* 2021b). For instance, the use of receiver functions can provide estimates of the variation of the Vp/Vs ratio and crustal thickness in a given area, although a reference velocity model is required for estimating the ray path and nominal velocity structure.

With the aim of combining these two seismic observation strategies that could form mutual confirmations, we conceived a seismic experiment that could simultaneously collect both seismic data sets. However, there was a mismatch of observation modes between the two observation systems. Meanwhile, the use of dense seismic

arrays of short-period seismometers for passive-source based exploration has received much attention over the last few years (Niu & Li 2011; Schulte-Pelkum & Mahan 2014; Wang *et al.* 2016; Liu *et al.* 2017). Unlike using broad-band seismometers, whose stations are usually spaced up to 10 km or more apart (to reduce costs), the deployment of a large number of instruments with a short spacing (from approximately hundreds of metres to 1 km) can improve the resolution of tomographic images and reduce costs (Yu *et al.* 2020). Therefore, conducting a WARR profile with a dense short-period seismic array might be beneficial. The observational coordination and its practicability have led us to combine active- and passive-source seismic exploration by applying the WARR method and the receiver function method to data collected from the same profile. In this way, we can obtain information on seismic velocities, intracrustal interfaces and the Vp/Vs ratio synchronously, which can help us to better understand the regional geodynamics.

We chose the Cathaysia Block as the target area to implement our research strategy. As part of the South China Block (SCB), the Cathaysia Block is located in southeastern China (Fig. 1) and has undergone multiple episodes of deformation, metamorphism and magmatic events from the Palaeoproterozoic to the Mesozoic (Shu *et al.* 2015). The widespread igneous province (Fig. 1) induced by the tectono-thermal activities in the Cretaceous was dominated by crustal extension (Zhou *et al.* 2006). The Qinhang Metallogenic Belt (QMB) and the Wuyishan Metallogenic Belt (WMB), located in the Cathaysia Block, were formed following these tectonic activities (delimited by dashed lines in Fig. 1). The crustal thickness, distribution of *P*-wave velocity and Vp/Vs ratio can provide tight constraints on mineralization and its geodynamic processes (Lin *et al.* 2021). All these features inspired us to select the Cathaysia Block as the study site for conducting joint active- and passive-source seismic experiments that cover both important metallogenic belts. Furthermore, the Cathaysia Block has been subjected to an extensional tectonic regime since the early Yanshanian Period (180–142 Ma) as a result of tectonic events related to upwelling of the asthenosphere and heating of the lithosphere (Zhou & Li 2000; He & Xu 2012; Liu *et al.* 2015). In the framework of continuous extensional stress, the lithosphere underwent thinning from 110–230 up to 60–70 km (Liu *et al.* 2012; Li *et al.* 2013; Wang *et al.* 2013; Ye *et al.* 2014; Shan *et al.* 2017; Deng & Levandowski 2018). Subsequently, the crust underwent reconfiguration and thinning to a ∼30 km thickness (Zhang *et al.* 2013a; Li *et al.* 2015; Cai *et al.* 2016; Kuo *et al.* 2016). Since the WARR method can provide Vp information and the receiver function method is more sensitive to the Vp/Vs ratio, the combined application of these two methods could give us an improved quantification of crustal properties. To take advantage of these possibilities, we followed a working scheme that first used the average *P*-wave velocity obtained by the WARR method to define a local background velocity model and then applied receiver functions imaging methods for a more reasonable result and explanation of the crust in SE China.

2 DATA AND METHODS

2.1 Data acquisition

To carry out the joint seismic experiment, from November to December 2018, we deployed a 530-km-long NW–SE-trending dense linear seismic array from Wanzai to Yongchun in SE China. A total of 435 three-component, short-period seismometers (blue triangles in Fig. 1) with a cut-off frequency of ∼2 Hz were installed along

the profile, with a spacing of approximately 1.0–1.5 km. Four shots (red stars in Fig. 1) were fired along the profile at approximately 80–90 km intervals. The explosive charge of each shot varied from 2000 to 2520 kg. Likewise, we also passively recorded for teleseismic events (see middle right inset in Fig. 1) for 28 days.

Earlier, during the period from June to August 2012, the Fujian Province Earthquake Administration conducted a 270-km-long WARR profile from Ninghua to Hui'an (which overlaps with our profile from Ninhua to Yongchun, Fig. 1) to study the deep structure of the SE margin in mainland China (Cai *et al.* 2016). The seismic receivers were deployed with a spacing of approximately 1.5–2.0 km, and five shots were detonated at approximately 50–98 km intervals (numbered Sp21–Sp25 in Fig. 9). Fig. 2 shows in detail the complete data capture system.

2.2 Images obtained using receiver functions

2.2.1 Data preparation

As usual, we considered the differences in traveltimes of the direct and converted waves (delay times) to characterize the medium and its seismic velocity structure with receiver functions. Accordingly, we chose 10 teleseismic events with magnitude $M_w \geq 6.0$ (Fig. 1) to gather original seismic signals with a high signal-to-noise ratio (SNR) and thereby high-quality receiver functions. First, we resampled the signals with a sampling rate of 20 Hz and removed the instrumental response from the frequency band of interest. Then, we rotated the Z-N-E components to the Z-R-T coordinate system and applied a time-domain iterative deconvolution (Ligorría & Ammon 1999) to calculate the *P*-wave receiver functions with a low-pass Gaussian filter. In particular, we selected 4.0 as the value of the Gaussian parameter α, which implied a high cut-off frequency of approximately 2.2 Hz, which matched the cut-off frequency of the instruments. Finally, after moveout correction and manual selection, we collected 3960 receiver functions.

2.2.2 *H–κ* stacking

Next, we adopt the *H–κ* stacking method (Zhu & Kanamori 2000) to calculate the average crustal thickness *H* and the Vp/Vs ratio below each seismic station. This algorithm is based on the delay time between the respective arrivals of the *P* and *Pms* waves. Therefore, these phases in combination with the multiple *PpPs* and *PpSs* + *PsPs* phases must appear very clear in the receiver functions. In this regard, Fig. 3 shows the receiver functions for each station of the array that were computed from the waveforms generated by two teleseismic events: one of magnitude M_w 7.1 located in Alaska and another of an M_w 7.5 magnitude located in New Caledonia. All *Pms* arrivals ranged from 3.5 to 4.0 s. Fig. 4 shows the stacked receiver functions for each station in the 0–20 s time range: arrivals corresponding to the *Pms* were all within the 3.5–4.0 s time interval (phase 1 on the right), while the arrivals of the *PpPs* and *PpSs* + *PsPs* phases were approximately 13 s (phase 2) and 17 s (phase 3), respectively.

The accuracy of the background velocity model used with this method is an important requirement. Some global velocity models may not work well for studying a given area. Fortunately, a previous study provided us with local WARR results for reference (Cai *et al.* 2016; Lin *et al.* 2021). Table S1 (Supporting Information) contains a partial reference *P*-wave velocity model for the extended Wanzai
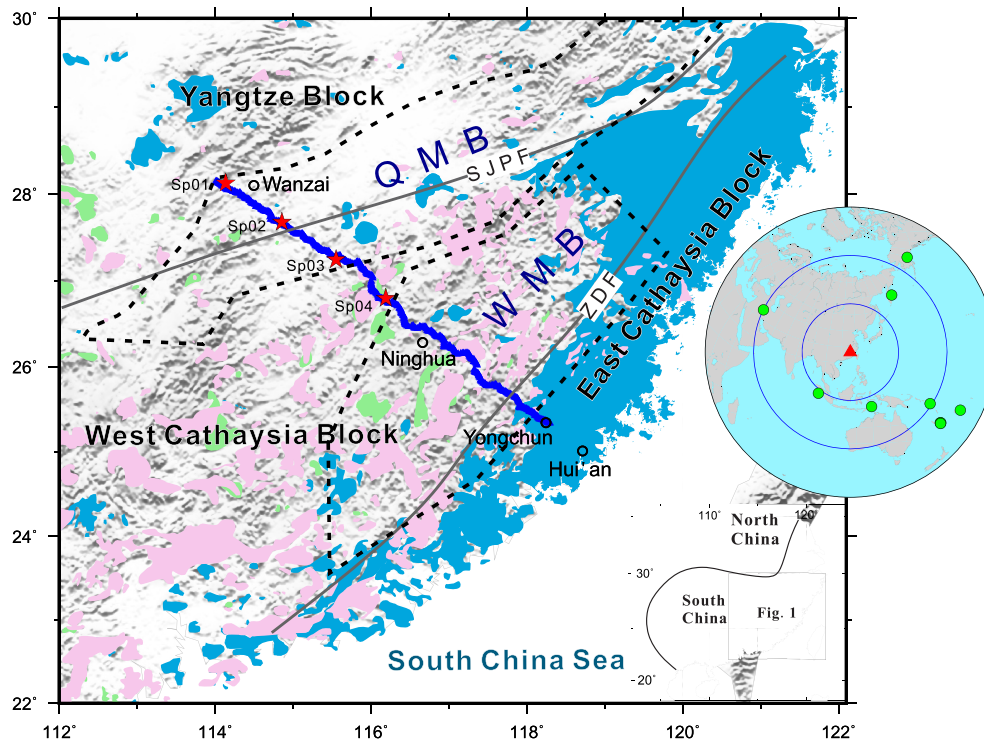
Figure 1. Map showing the regional geology and the location of the active- and passive-source seismic profile. Red stars represent shot points (Sp01–Sp04), while blue triangles show short-period seismic stations deployed on the terrain. Igneous rocks (after Zhou *et al.* 2006): oldest Indosinian granitoids (251–205 Ma, light green areas); early Yanshanian granitoid-volcanic rocks (180–142 Ma, pink areas); late Yanshanian granitoid-volcanic rocks (142–67 Ma, light blue areas). Faults: SJPF, Shaoxing-Jiangshan-Pingxiang fault; ZDF, Zhenghe-Dapu fault. Metallogenic Belts: QMB, Qinhang Metallogenic Belt; WMB, Wuyishan Metallogenic Belt. Middle right inset map: location of the seismic events used in this study on a worldwide map (green circles); the red triangle denotes the approximate location of the seismic array. Lower right corner inset map shows the location of the study area.
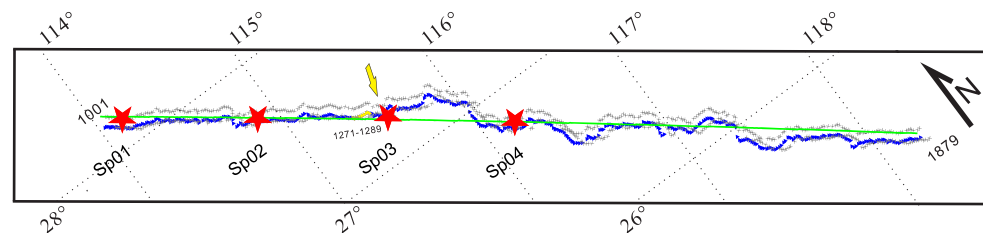

Figure 2. The seismic source and receiver network in detail. Red stars represent shot points (Sp01–Sp04), while blue triangles (numbered from 1001 to 1879 and spaced ∼1 km apart) show short-period seismic stations deployed on the terrain. Yellow triangles (near the Sp03 shot point) indicate the set of stations 1271 to 1289. The yellow arrow marks the position of station 1307. The line formed by grey crosses stands for the projections of piercing points of converted waves at 30 km depth, calculated with the iasp91 model (Kennett & Engdahl 1991). The green line indicates the position of the image obtained in this study.

to Yongchun profile that was constructed from the available WARR data set.

To implement *H–κ* stacking with the Moho converted *Pms* phase, the *PpPs* phase and the multiple *PpSs + PsPs* phase, we started with the high-SNR signals generated by the four aforementioned teleseismic events. We used a grid search to construct the variance diagram for *H* and Vp/Vs, using step sizes of 0.05 km and of 0.025, respectively. The three mentioned seismic phases allowed us to check the consistency of the results. For example, in Fig. 5, we show the stacked receiver functions at four central stations, 1173, 1333, 1529 and 1715, and in Fig. 6 we show the results for these stations. The variance diagrams for each of these stations after using the *Ps*, *PpPs* and *PpSs + PsPs* phases are shown in four plots; the fourth plot (lower right corner) shows the variance diagram obtained from the stacked amplitudes provided by the former three phases. In all cases, the maximum amplitudes observed in these diagrams

(white stars in the graphs) provide a solution for the thickness of the crust and the Vp/Vs ratio below the reference station. All of these solutions were observed to represent high likelihood maxima in the search space.

To check the consistency of the results, we first perform *H–κ* stacking of receiver functions by taking the radius of 20 adjacent stations along the profile and using the iasp91 model (Kennett & Engdahl 1991) to obtain the variation of the Vp/Vs ratio and the crustal thickness (Fig. 7a). Next, we repeated the same stacking operation using a radius of 40 adjacent stations (and the iasp91 model too) to minimize the effects of any abrupt variation below each station and large-scale anomalies (Fig. 7b). Finally, we conducted *H–κ* stacking using the background WARR velocity model (Supporting Information Table S1) determined by Lin *et al.* (2021) and Cai *et al.* (2016) instead of the iasp91 model, modified by the *H–κ* stacking result with a stacking radius of 40 adjacent stations to achieve more
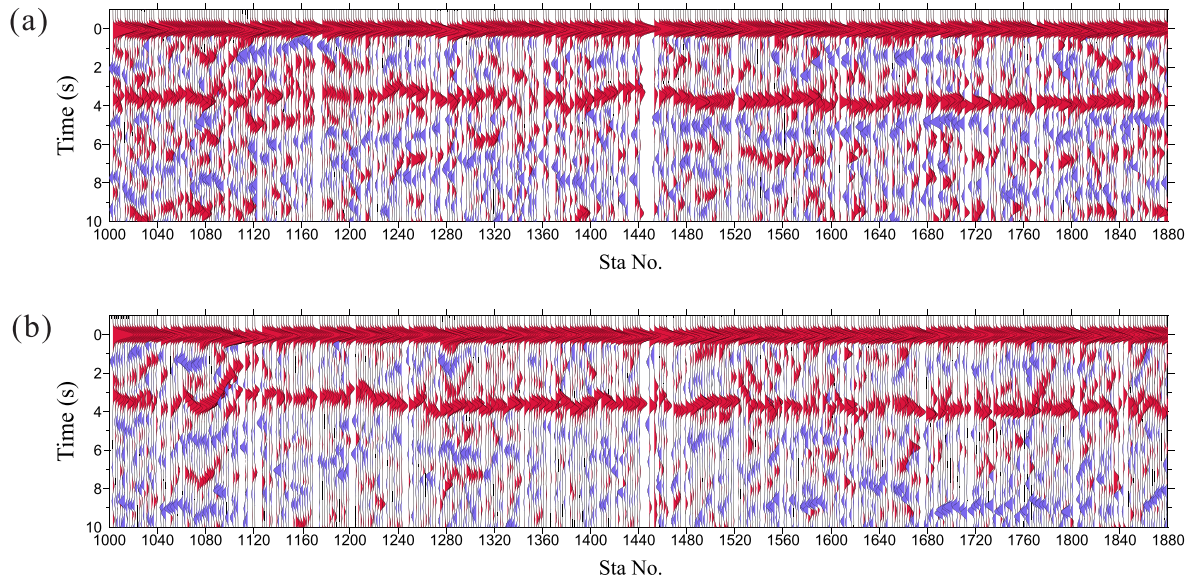
(a)

(b)

Figure 3. Receiver functions for each station computed from the waveforms generated by two teleseismic events: (a) one of magnitude M_w 7.1 located in Alaska and (b) another of magnitude M_w 7.5 located in New Caledonia. Delay time on the vertical axis and numbered stations on the horizontal axis.
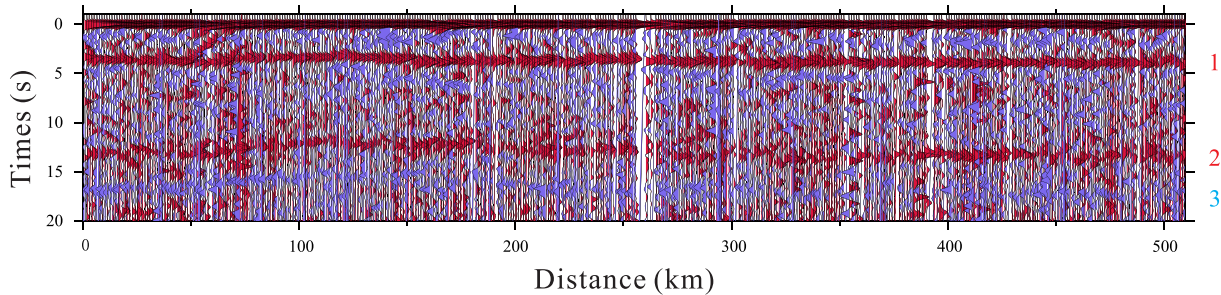

Figure 4. Stacked receiver functions for each station. Arrivals within the time interval 3.5–4.0 s (phase 1 on the right) correspond to the *Pms* wave, while arrivals around 12.5 s (phase 2) and 17 s (phase 3) correspond to the *PpPs* and *PpSs + PsPs* phases, respectively.

(a) sta.1173

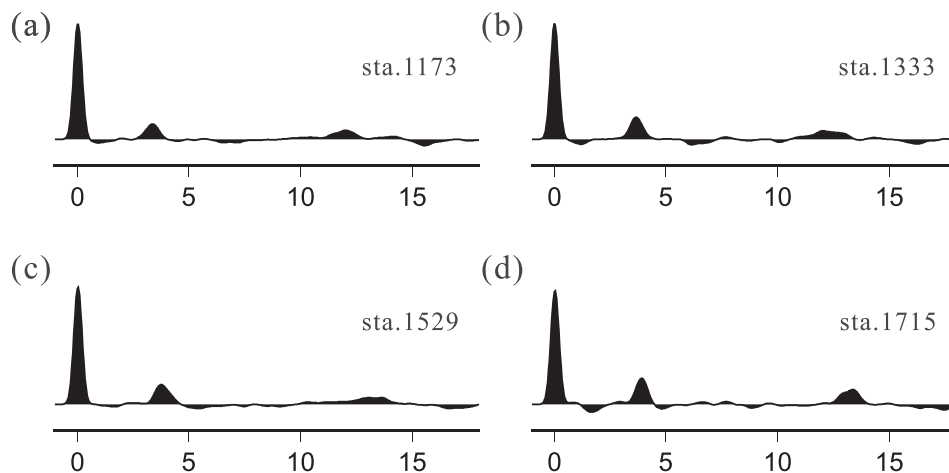(b) sta.1333

(c) sta.1529

(d) sta.1715

Figure 5. Stacked traces of receiver functions at four centre stations: (a) 1173; (b) 1333; (c) 1529; (d) 1715. These traces are used for the treatment of the *Ps*, *PpPs* and *PpSs + PsPs* phases (see Fig. 4). Delay time (seconds) on the *x*-axis.

accurate values of the Vp/Vs ratio and crustal thickness compared to those obtained with the iasp91 model (Fig. 7c). We observed a remarkable consistency between all these results, although the latter example showed smoother results and smaller error bars.

2.2.3 CCP images

We used the common conversion point (CCP) stacking method (Dueker & Sheehan 1998) to image intracrustal discontinuities from receiver functions. The piercing points of the *P*-to-*S* converted
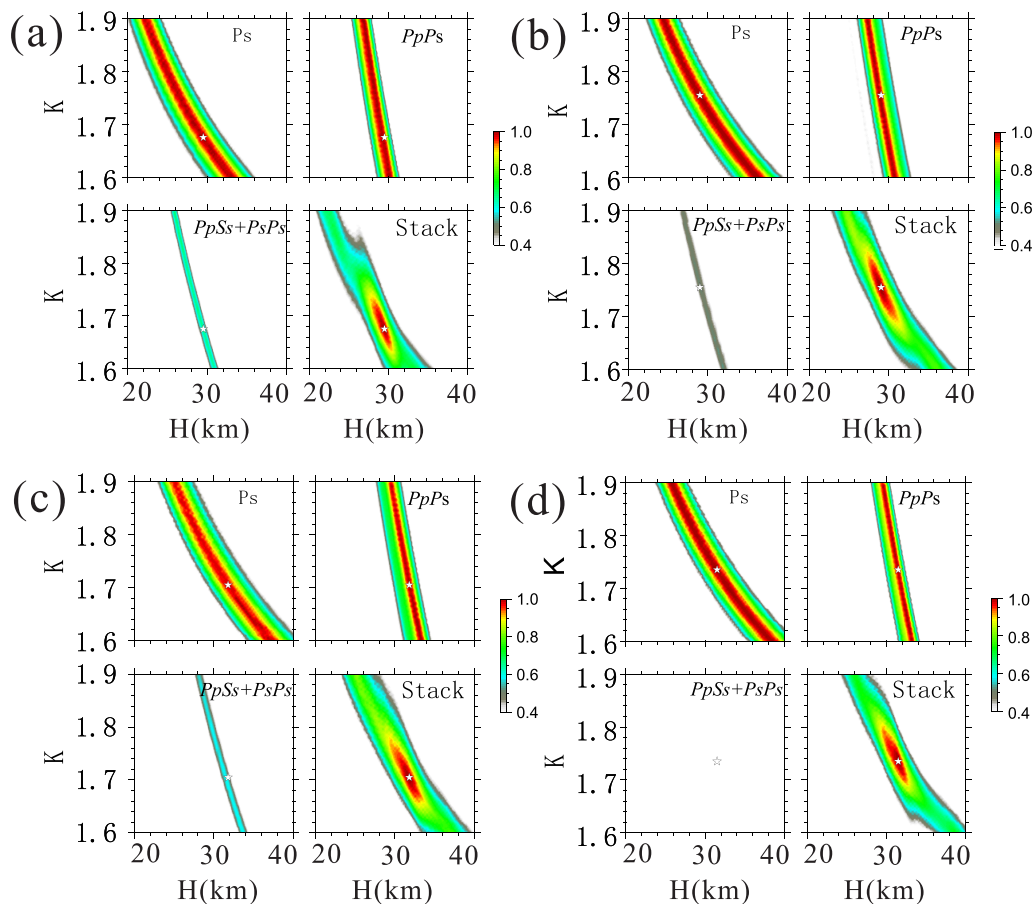
Figure 6. *H–κ* stacking results for four centre stations: (a) 1173; (b) 1333; (c) 1529; (d) 1715. For each centre station, four plots show the results obtained using the *Ps*, *PpPs* and *PpSs* + *PsPs* phases; the fourth plot (lower right corner) shows the variance diagram from the stacked amplitudes provided by the former three phases. In all cases, the white stars indicate the respective solutions for *H* and the Vp/Vs ratio.

waves were calculated with the iasp91 model (Kennett & Engdahl 1991) to a depth of 30 km (line formed by grey crosses in Fig. 2). Taking into account the spacing between each seismometer, the size of the bin box was set at 1.5 × 5.0 km² horizontally and 0.5 km vertically. By transferring the delay time between the converted *Ps* wave and the direct *Pp* wave to the depth domain, we obtained the amplitudes at each point that represent the seismic impedance change.

To obtain the common conversion points, we used the iasp91 model as the background velocity model for migration to the depth domain and the velocity model below each individual station provided by the WARR model (Lin *et al.* 2021) that was modified by the *H–κ* stacking result. In addition to the *Pms* wave, we performed migration using the *PpPs* multiple wave to check for consistency since the signals from the *PpSs* + *PsPs* phase were not strong enough at all receiver stations. Fig. 8 shows three CCP images along the Wanzai–Yongchun profile: the CCP image from *Pms* using the iasp91 model (Fig. 8a), the CCP image from *Pms* using the WARR velocity model modified by the *H–κ* stacking result (Fig. 8b), and the CCP image from *PpPs* using the WARR velocity model modified by the *H–κ* stacking result (Fig. 8c). The results obtained by *H–κ* stacking at all stations were also plotted for comparison (white dotted lines in the illustration). The maximum amplitudes obtained in the three cases coincided well, although the results from the CCP and *H–κ* stacking matched better when using the WARR model instead of the iasp91 model.

3 CRUSTAL STRUCTURE

3.1 *H–κ* stacking-based results

The thickness of the crust varies laterally along the Wanzai–Yongchun profile, thickening from the west to the east from 28 to 32 km and reaching its smallest value below the Yongfeng Basin (marked YFB in the top panels of Fig. 7). The crust is slightly thinner (approximately 28 km) in the northwest transect below the QMB and somewhat thicker (31–32 km) in the southeast segment below the WMB where it has an almost flat bottom. The average crustal thickness is about 31 km in SE China, which is consistent with the WARR results (Cai *et al.* 2016; Lin *et al.* 2021) and other passive-source seismic results (Li *et al.* 2013; Ye *et al.* 2013; Zhang *et al.* 2021a, 2022). Even so, the crust is thinner compared to the global average crustal thickness of shields and platforms, which is about 40 km (Christensen & Mooney 1995).

The results provided by *H–κ* stacking show that the mean value of the Vp/Vs ratio is approximately 1.71 along the reference profile (Fig. 7c), which is less than the global average value for the continental crust (1.768; Christensen 1996). All *H–κ* stacking results indicate that the average Vp/Vs ratio is higher in the WMB than in the QMB, except at distances of 20–60 and 140–180 km (Fig. 7). The lowest value of the Vp/Vs ratio, about 1.65, was observed in the central part of QMB, while the highest value of about 1.8 corresponds to YFB (Fig. 7 and Supporting Information Fig. S2). The Vp/Vs ratio shows an increasing trend from NW to SE throughout
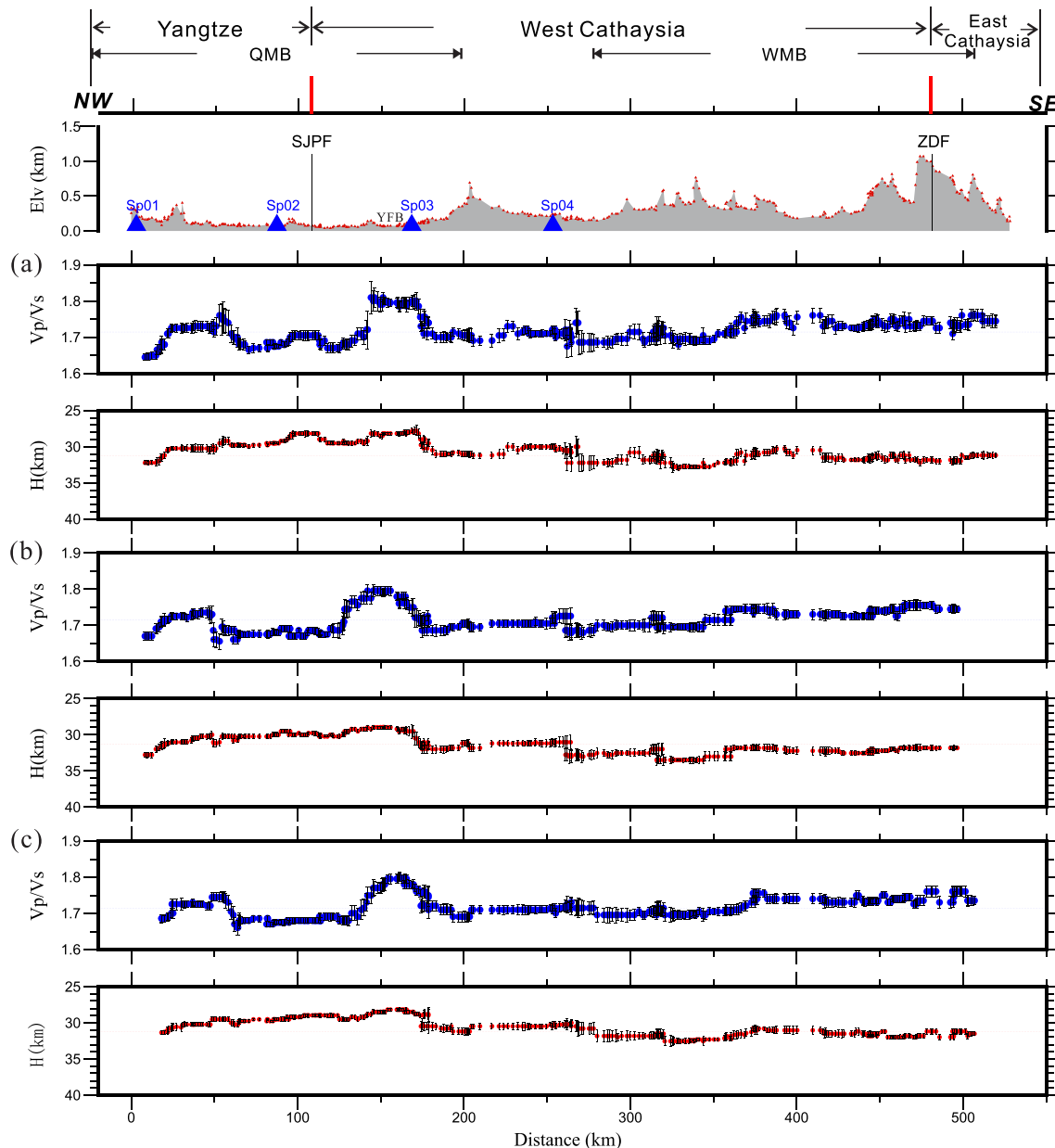
Figure 7. *H–κ* stacking results (Vp/Vs ratio and Moho depth, blue and red lines, respectively) for all stations. (a) *H–κ* stacking results using the background velocity provided by the iasp91 model (Kennett & Engdahl 1991), with a stacking radius of 20 adjacent stations. (b) Same using the iasp91 model and a stacking radius of 40 adjacent stations. (c) Same using the background velocity of the average WARR model (Lin *et al.* 2021) modified by the *H–κ* stacking result and a stacking radius of 40 adjacent stations. In all cases, the dotted lines indicate the mean values and the black bars the error bars. The two upper panels show the elevation of the array stations (small red triangles), the location of the shot points Sp01–Sp04 (blue triangles), as well the faults and tectonic units that the profile crosses. SJPF, Shaoxing-Jiangshan-Pingxiang fault; ZDF: Zhenghe-Dapu fault; YFB, Yongfeng Basin; QMB: Qinhang Metallogenic Belt; WMB: Wuyishan Metallogenic Belt.

the entire profile excluding the two anomalies mentioned above. Nevertheless, the relatively low Vp/Vs ratio may be evidence of a low content of mafic material in the crust.

3.2 CCP image-based results

The images of the crust provided by the CCP method after using the WARR *P*-wave velocity model (Lin *et al.* 2021) constrained by the *H-κ* stacking–based results (Fig. 7) allowed us to analyse the differences with the results supplied by the *H-κ* stacking of receiver functions. The maximum amplitude in the CCP image obtained

using the *Pms* phase and only the iasp91 model showed a deviation of the Moho of about 2–5 km (Fig. 8a), which can be attributed to the deviation of the reference model from the real model. However, the CCP images based on the *Pms* phase (Fig. 8b) or the *PpPs* phase (Fig. 8c), which used the WARR velocity model modified by the *H–κ* results, showed better consistency both in the amplitudes and in the Moho depth. In particular, the CCP image in Fig. 8(c) depicts the undulation of the Moho more clearly and shows a more prominent feature of the Moho uplift below the QMB. Furthermore, this image reflects a discontinuity at a depth close to 20 km, which also exists in the results provided directly by the WARR result.
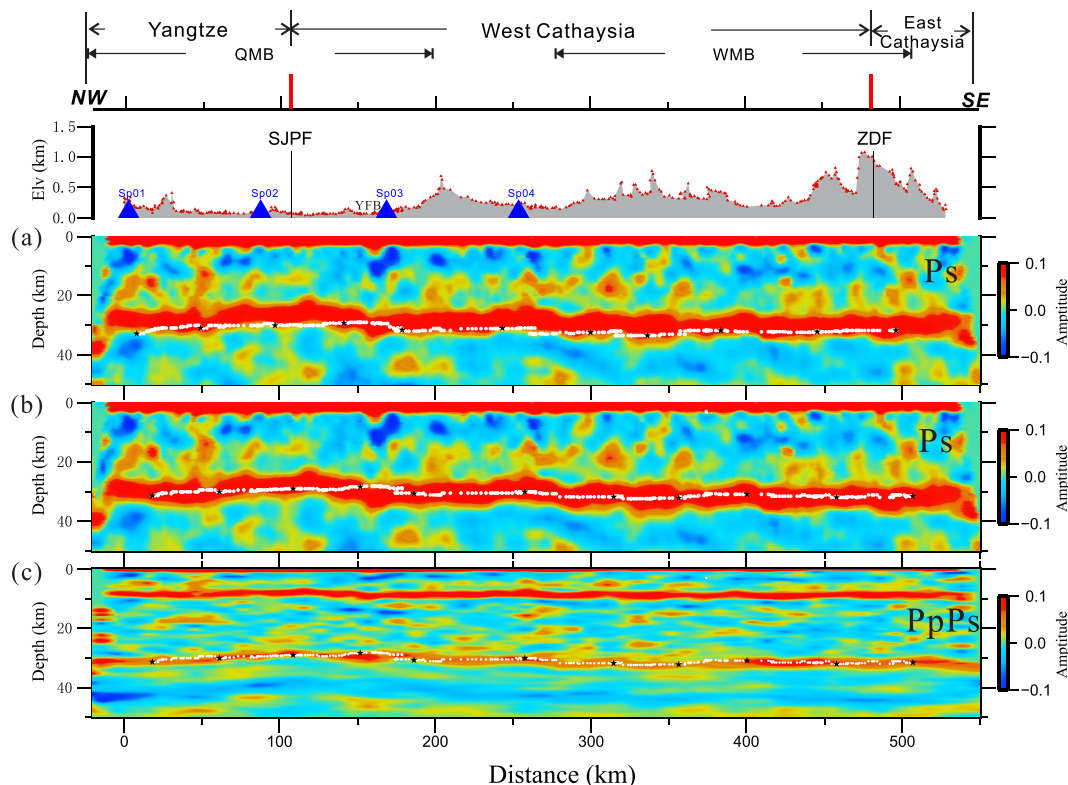
Figure 8. CCP images along the Wanzai–Yongchun seismic profile (amplitude scales on the right). (a) CCP image from *Pms* using the iasp91 model (Kennett & Engdahl 1991). (b) CCP image from Pms using the WARR velocity model (Lin *et al.* 2021) modified by the *H–κ* stacking result. (c) CCP image from *PpPs* using the WARR velocity model modified by the *H–κ* stacking result. Black stars indicate the results of *H–κ* stacking at some of the centre stations. The white dotted lines indicate the results of *H–κ* stacking at the array stations. The two upper panels show the elevation of the array stations (small red triangles), the location of the shot points Sp01–Sp04 (blue triangles), as well the faults and tectonic units that the profile crosses. QMB: Qinhang Metallogenic Belt; WMB: Wuyishan Metallogenic Belt; SJPF, Shaoxing-Jiangshan-Pingxiang fault; ZDF: Zhenghe-Dapu fault; YFB, Yongfeng Basin.

Validation tests supporting the consistency of the receiver functions and addressing the potential effect of sediments on the results are included in the Supporting Information (Figs S1 and S2).

4 DISCUSSION

4.1 Comparison with previous results

In Fig. 9 we show a vertical section of the crust along the Wanzai–Yongchun profile in SE China. The Moho discontinuity along the Wanzai–Yongchun profile revealed by *H–κ* stacking matches well with the WARR model (Lin *et al.* 2021), except for some small-scale deviations that may result from disagreement between the *Pms* piercing points and the lack of ray coverage in some particular area when applying the WARR method (Figs 2 and 9). The Ninghua-to-Hui'an WARR profile performed by Cai *et al.* (2016), which overlaps with our profile by 195 km, progressively shows a shallower Moho from the mainland towards the coast, with a depth of 31.8 km below the WMB up to 28.4 km at the eastern end of the profile. The Shaowu-to-Pingtan WARR transect studied by Li. *et al.* (2015) shows a slightly deeper Moho than that reflected by our profile, about 33.0 km deep inland and 30.0 km to the southeast. Another 400-km-long southeast trending WARR profile from Lianxian to Guangkou, reveals that the Moho depth ranges from 34 to 32 km in the NW–SE direction (Zhang & Wang 2007; Zhang *et al.* 2013b). All these WARR results demonstrate that the crustal

thickness is approximately 28–34 km in the Cathaysia Block, gradually thinning as we approach the coast from inland. Regardless, the average thickness of the crust indicated by several studies is approximately 31 km, which is in agreement with the values provided by the model obtained from receiver functions and CCP images (Figs 7 and 8). Additionally, the Moho uplift (approximately 2–3 km) beneath the QMB in the northwestern segment of our profile is visible in the *H-κ* stacking results (Fig. 7). We conclude that the joint active- and passive-source experiment described here provides an opportunity to take a closer look at the reshaped crust of the SCB. The expanded database and the background velocity model supported by the WARR data lead to an improved image of the crust with clearer velocity changes.

Previous studies based on receiver functions provide additional results, including the Vp/Vs ratio. Thus, the results obtained from 44 broad-band seismographs deployed in Fujian and Taiwan provinces indicate that the thickness of the crust in Fujian province ranges from 28.3 to 32.8 km and that the Vp/Vs ratio varies from 1.70 to 1.84, with a mean value of 1.76 (Ai *et al.* 2007). Other results derived from receiver functions show that the Vp/Vs ratio varies from 1.72 to 1.83 along the coast, with a mean value of 1.78 (Li *et al.* 2013; Ye *et al.* 2013; Ye *et al.* 2014). The joint inversion of receiver functions and vertical gravity gradient data measured at 245 permanent seismic stations installed in South China (Guo *et al.* 2019) also confirms a crustal thickness of 28–32 km and a Vp/Vs ratio of 1.7–1.8 along the profile in this paper.
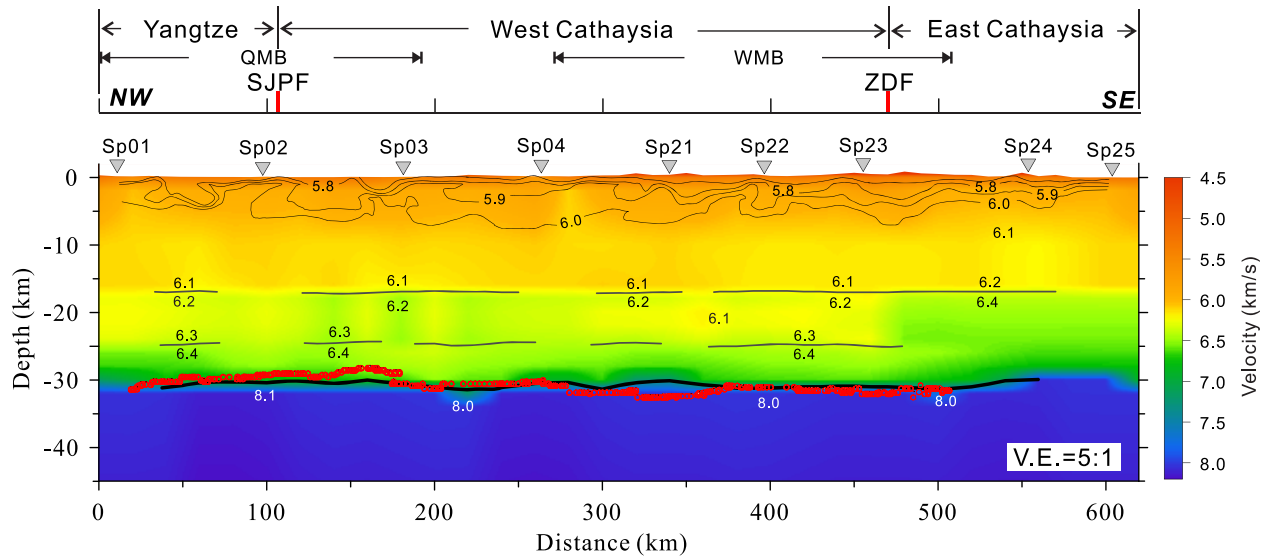
Figure 9. Comparison of the Moho depth revealed by *H–κ* stacking (red circles) and the WARR model (thick black line) along the Wanzai–Yongchun profile in SE China (inverted triangles Sp01–Sp25 represent shot points). Numbers indicate *P*-velocity values (scale on the right). The top panel shows the faults and tectonic units that the profile crosses. QMB: Qinhang Metallogenic Belt; WMB: Wuyishan Metallogenic Belt; SJPF, Shaoxing-Jiangshan-Pingxiang fault; ZDF: Zhenghe-Dapu fault.
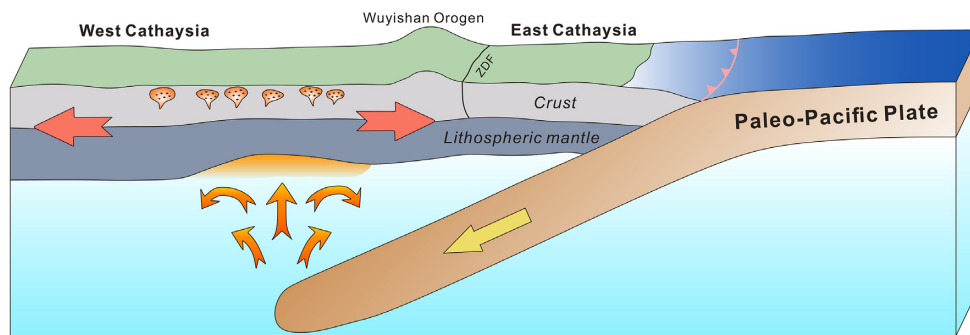

Figure 10. Schematic illustrating the crust-mantle tectonic evolution in southeastern China associated with the subduction of the Paleo-Pacific plate since the Late Mesozoic (ZDF is the Zhenghe-Dapu fault).

These results agree with ours and reveal that the Vp/Vs ratio is much higher in places close to the coast (approximately 1.76–1.80) than inland (1.70–1.76), with the exception of some small-scale anomalies. Considering the sparse deployments of broad-band stations (every 30–50 km), our dense network of short-period instruments (with seismometers spaced ∼1.0 km) allows us to obtain a higher lateral resolution image in terms of crustal thickness and Vp/Vs ratio. This is justified because we use a more precise P-wave velocity deduced from WARR data, *H*-κ stacking and CCP images, which improves the accuracy of the results.

4.2 Crust thickness variation along the East Yangtze Block and the Cathaysia Block

The western part of the Yangtze Block looks more like a craton and has a Moho depth of approximately 45–50 km (Li *et al.* 2013; Ye *et al.* 2014). However, as we leave the West Yangtze Block and approach the area where it merges with the West Cathaysia Block along its eastern boundary, the crustal thickness shows significant difference. Thus, the thickness of the crust reaches a minimum value of ∼28 km around the Shaoxing-Jiangshan-Pingxiang fault (SJPF) that separates the two blocks (Fig. 1).

Other geophysical studies also show that the thickness of the lithosphere in eastern China has clearly changed since the Mesozoic (Chen *et al.* 2008; ; Deng & Levandowski 2018). Large-scale thinning of the crust and lithosphere could have originated from the subduction of the Paleo-Pacific plate (Dong *et al.* 2020), but the dominant intracontinental orogeny in the SCB intensified this action, especially along the SJPF.

4.3 Variation of the Vp/Vs ratio: implications for the SCB

The mean value of the Vp/Vs ratio we determined for the crust is 1.71, which is relatively low when compared to the global continental standard (Christensen & Mooney 1995; Christensen 1996). Furthermore, there is a positive correlation between the thickness of the crust and the Vp/Vs ratio: a thinner crust corresponds to a lower Vp/Vs ratio (western half of the profile), while a thicker crust corresponds to a higher Vp/Vs ratio (eastern half of the profile). This also correlates with the elevation of the array stations (less in the northwestern section and more in the southeastern section).

Combining this result with the large-scale thinning of the crust in the SCB and the 2D WARR velocity model (Lin *et al.* 2021), we can speculate that the crust as a whole has a deficit of mafic material.

The variation of the Vp/Vs ratio near the SJPF in the Yangtze Block appears to be stronger, suggesting that intracontinental orogeny aggravated the remodelling of the crust.

An extension of the crust or a crustal delamination process can be accompanied by the backarc subduction of the Paleo-Pacific plate since the Late Mesozoic (Fig. 10). The induced extensional stress and magmatic activity could break the balance between the lower crust and the mantle to produce a flat and slightly thinned crust in the Cathaysia Block.

5 CONCLUSIONS

Based on the joint seismic observation experiment across the Cathaysia Block, we obtain a passive-source seismic result of the crust with robust *P*-wave velocity support from active-source seismic data acquisition and draw the following conclusions:

(1) The thickness of the crust varies laterally from west-to-east from 28 km below the QMB to 32 km below the WMB. The Vp/Vs ratio of the crust has an average value of 1.71. Both the crustal thickness and the mean Vp/Vs ratio are lower than the standard values for the continental crust.

(2) A relatively thin crust and its low Vp/Vs ratio of the Cathaysia Block indicate that it has a deficit of mafic material, which may result from the thinning of the lower crust, dominated by the extensional stress background resulting in the subduction of the Paleo-Pacific plate.

(3) The implemented seismic data analysis technique, based on dense short-period data processing and receiver functions, acquires a preliminary exploration of crustal imaging methods, and its complementarity and coordination reveal a further potential for a seismic observation mode.

DATA AVAILABILITY

The data used in this study are available from the IGGCAS with license restrictions, so it is not yet publicly available. We declare that this paper has not been submitted elsewhere.

CONFLICT OF INTEREST

The Author declare that there is no conflict of interest.

REFERENCES

Ai, Y., Chen, Q., Zeng, F., Hong, X. & Ye, W., 2007. The crust and upper mantle structure beneath southeastern china, *Earth planet. Sci. Lett.,* **260,** 549–563.

Bao, X., Song, X. & Li, J., 2015. High-resolution lithospheric structure beneath Mainland China from ambient noise and earthquake surface-wave tomography, *Earth planet. Sci. Lett.,* **417,** 132–141.

Cai, H., Jin, X., Wang, S., Li, P. & Chen, W., 2016. The crust structure and velocity structure characteristics beneath Ninghua-Datian-Hui'an, *Chin. J. Geophys.,* **59**(1), 157–168 (in Chinese with abstract in English).

Chen, L., Tao, W., Zhao, L. & Zheng, T., 2008. Distinct lateral variation of lithospheric thickness in the northeastern North China craton, *Earth planet. Sci. Lett.,* **267**(1-2), 56–68.

Christensen, N.I., 1996. Poisson's ratio and crustal experiment, *J. geophys. Res.,* **101**(B2), 3139–3156.

Christensen, N.I. & Mooney, W.D., 1995. Seismic velocity structure and composition of the continental crust: a global view, *J. geophys. Res.,* **100**(B7), 9761–9788.

Deng, Y. & Levandowski, W., 2018. Lithospheric alteration, intraplate crustal deformation, and topography in eastern China, *Tectonics,* **37,** 4120–4134.

Dong, S., Li, J., Cawood, P.A., Gao, R., Zhang, Y. & Xin, Y., 2020. Mantle influx compensates crustal thinning beneath the Cathaysia Block, South China: evidence from SINOPROBE reflection profiling, *Earth planet. Sci. Lett.,* **544**(2020), 116360.

Dueker, K.G. & Sheehan, A.F., 1998. Mantle discontinuity structure beneath the Colorado Rocky Mountains and High Plains, *J. geophys. Res.,* **103**(B4), 7153–7169.

Guo, L., Gao, R., Shi, L., Huang, Z. & Ma, Y., 2019. Crustal thickness and Poisson's ratios of South China revealed from joint inversion of receiver function and gravity data, *Earth planet. Sci. Lett.,* **510,** 142–152.

He, C., Dong, S., Santosh, M. & Chen, X., 2013, Seismic evidence for a geosuture between the Yangtze and Cathaysia blocks, South China, *Sci. Rep.,* **3**(29), 2200.

He, R., Shang, X., Yu, C., Zhang, H., Robert, D.& & Van der Hilst, R.D., 2014, A unified map of Moho depth and Vp/Vs ratio of continental China by receiver function analysis, *Geophys. J. Int.,* **199**(3), 1910–1918,

He, Z. & Xu, X., 2012. Petrogenesis of the Late Yanshanian mantle-derived intrusions in southeastern China: response to the geodynamics of Paleo-Pacific plate subduction, *Chem. Geol.,* **328,** 208–221.

Kennett, B.L.N. & Engdahl, E.R., 1991. Traveltimes for global earthquake location and phase identification, *Geophys J. Int.,* **105**(2), 429–465.

Kuo, Y., Song, X., Kuo-Chen, H., Jin, X., Cai, H., Lin, J., Wu, F., Yen, H., Huang, B., Liang, W., Okaya, D. & Brown, L., 2016. Crustal structures from the Wuyi-Yunkai orogen to the Taiwan orogen: the onshore-offshore wide-angle seismic experiments of the TAIGER and ATSEE projects, *Tectonophysics,* **692,** 164–180.

Li, P., Jin, X., Wang, S. & Cai, H., 2015. Crustal velocity structure of the Shaowu-Nanping-Pingtan transect through Fujian from deep seismic sounding-tectonic implications, *Sci. China: Earth Sci.,* **45,** 1757–1767 (in Chinese with abracst in English).

Li, Q., Gao, R., Wu, F., Guan, Y., Ye, Z., Liu, Q., Hao, K., He, R., Li, W. & Shen, X., 2013. Seismic structure in the southeastern China using teleseismic receiver functions, *Tectonophysics,* **606,** 24–35.

Ligorría, J.P. & Ammon, C.J., 1999. Iterative deconvolution and receiver-function estimation, *Bull. seism. Soc. Am.,* **89**(5), 1395–1400.

Lin, J., Xu, T., Cai, H., LÜ, Q., Bai, Z., Deng, Y., Zhang, Y., Huang, M., Badal, J. & Jin, X., 2021. Crustal velocity structure of Cathaysia block from an active-source seismic profile between Wanzai and Hui'an in SE China. *Tectonophysics,* **811,** 228874.

Liu, C., Liu, Z., Wu, F. & Chu, Z., 2012. Mesozoic accretion of juvenile subcontinental lithospheric mantle beneath South China and its implications: geochemical and re-Os isotopic results from Ningyuan mantle xenoliths. *Chem. Geol.,* **291,** 186–198.

Liu, L., Xu, X. & Xia, Y., 2015. Asynchronizing paleo-Pacific slab rollback beneath SE China: insights from the episodic Late Mesozoic volcanism, *Gondwana Res.,* **37,** 397–407.

Liu, Z., Tian, X., Gao, R., Wang, G., Wu, Z., Zhou, B., Tan, P., Nie, S., Yu, G., Zhu, G. & Xu, X., 2017. New images of the crustal structure beneath eastern Tibet from a high-density seismic array, *Earth planet. Sci. Lett.,* **480,** 33–41.

Niu, F. & Li, J., 2011. Component azimuths of the CEArray stations estimated from P-wave particle motion, *Earthq. Sci.,* **24,** 3–13.

Schulte-Pelkum, V. & Mahan, K.H., 2014. A method for mapping crustal deformation and anisotropy with receiver functions and first results from USArray, *Earth planet. Sci. Lett.,* **402,** 221–233.

Shan, B., Xiong, X., Zhao, K., Xie, Z., Zheng, Y. & Zhou, L., 2017. Crustal and upper-mantle structure of South China from Rayleigh wave tomography, *Geophys. J. Int.,* **208,** 1643–1654.

Shu, L., Wang, B., Cawood, P.A., Santosh, M. & Xu, Z., 2015. Early Paleozoic and Early Mesozoic intraplate tectonic and magmatic events in the Cathaysia block, South China, *Tectonics,* **34,** 1600–1621.

Wang, X., Chen, Q., Li, J. & Wei, S., 2016. Seismic sensor misorientation measurement using p-wave particle motion: an application to the necsaids array, *Seismol. Res. Lett.,* **87**(4), 901–911.

Wang, Y., Zhang, A., Fan, W., Zhang, Y. & Zhang, Y., 2013. Origin of paleosubduction-modified mantle for Silurian gabbro in the Cathaysia Block: geochronological and geochemical evidence. *Lithos,* **160-161,** 37–54.

Ye, Z., Li, Q., Gao, R., Guan, Y., He, R., Wang, H., Lu, Z., Xiong, X. & Li, W., 2013. Seismic receiver functions revealing crust and upper mantle structure beneath the continental margin of southeastern China, *Chin. J. Geophys.,* **56**(9), 2947–2958 (in Chinese with abstract in English).

Ye, Z., Li, Q., Gao, R., Zhang, H., He, R., Wang, H. & Li, W., 2014. A thinned lithosphere beneath coastal area of southeastern China as evidenced by seismic receiver functions, *Sci. China: Earth Sci.,* **57,** 2835–2844 (in Chinese with abstract in English).

Yu, G., Xu, T., Ai, Y., Chen, L. & Yang, J., 2020. Significance of crustal extension and magmatism to gold deposits beneath Jiaodong Peninsula, eastern North China Craton: seismic evidence from receiver function imaging with a dense array, *Tectonophysics,* **789,** 228532.

Zhang, G., Guo, A., Wang, Y., Li, S., Dong, Y., Liu, S., He, D., Cheng, S., Lu, R. & Yao, A., 2013a. Tectonics of South China continent and its implications. *Sci. China: Earth Sci.,* **56,** 1804–1828 (in Chinese with abstract in English).

Zhang, Z., Xu, T., Zhao, B. & Badal, J., 2013b. Systematic variations in seismic velocity and reflection in the crust of Cathaysia: new constraints on intraplate orogeny in the South China continent, *Gondwana Res.,* **24,** 902–917.

Zhang, Y., Shi, D., Lü, Q., Xu, Y., Xu, Z., Yan, J., Chen, C. & Xu, T., 2021a. The crustal thickness and composition in the eastern South China Block constrained by receiver functions: Implications for the geological setting and metallogenesis, *Ore Geol. Rev.,* **130**(1), 103988.

Zhang, Y., Lü, Q., Yan, J., Xu, Y., Lin, J., Pi, J., Chen, M. & Zhang, W., 2022. Crustal structure of the middle segment of the Jiangnan Orogen and its implications on mineralization: Revealed by teleseismic receiver functions along the Guangchang-Liuyang profile, *Acta Petrologica Sinica,* **38**(2), 559–572 (in Chinese with abstract in English).

Zhang, Y., Shi, D., Lü, Q., Xu, Y., Xu, Z., Gong, X., Yan, J. & Xu, T., 2021b. A fine crustal structure and geodynamics revealed by receiver functions along the Guangchang-Putian line in the Cathaysia Block, South China, *Tectonophysics,* **815,** 229007.

Zhang, Z. & Wang, Y., 2007. Crustal structure and contact relationship revealed from deep seismic sounding data in South China, *Phys. Earth planet. Inter.,* **165,** 114–126.

Zheng, T., He, Y., Yang, J. & Zhao, L., 2015. Seismological constraints on the crustal structures generated by continental rejuvenation in northeastern china, *Sci. Rep.,* **5**(1), 14995.

Zhou, L., Xie, J., Shen, W., Zheng, Y., Yang, Y., Shi, H. & Ritzwoller, M.H., 2012. The structure of the crust and uppermost mantle beneath South China from ambient noise and earthquake tomography, *Geophys. J. Int.,* **189**(3), 1565–1583,

Zhou, X. & Li, W., 2000. Origin of Late Mesozoic igneous rocks in southeastern China: implications for lithosphere subduction and underplating of mafic magmas, *Tectonophysics,* **326**(3-4), 269–287.

Zhou, X., Sun, T., Shen, W., Shu, L. & Niu, Y., 2006. Petrogenesis of Mesozoic granitoids and volcanic rocks in South China: a response to tectonic evolution. *Episodes,* **29**(1), 26–33.

Zhu, L. & Kanamori, H., 2000. Moho depth variation in southern California from teleseismic receiver functions, *J. geophys. Res.,* **105,** 2969–2980.

SUPPORTING INFORMATION

Supplementary data are available at *GJI* online.

Figure S1. Receiver functions at centre stations 1371 (a) and 1505 (b). There are approximately 140 receiver functions in both cases. The respective stacked traces are shown on top.

Figure S2. (a) Receiver functions at station NE20 of NCISP-6 located in the Songliao basin, NE China (Zheng *et al.* 2015), to compare with the receiver functions at stations 1271–1289 (highlighted in yellow in Fig. 2) located in the Yongfeng basin, SE China. The two vertical dashed lines allow seeing the position of the peaks of the direct P wave with respect to the zero instant. (b) H–κ plots using stations 1271–1289 (not station 1307) and Ps, $PpPs$ and $PpSs + PsPs$ phases; also, H–κ plot using centre station 1307 alone (whose position is indicated by a yellow arrow in Fig. 2) and the stacked trace included on top of the graph. In all cases, the white star indicates the solution for the thickness of the crust and the Vp/Vs ratio.

Table S1. Reference P-wave velocity model for the extended Wanzai to Yongchun profile constructed from the available WARR data set (Cai *et al.* 2016; Lin *et al.* 2021). Horizontal distance and depth in km; Vp velocity in km s^{-1}. The numbers on the bottom row indicate Moho depths for different offsets.

Please note: Oxford University Press is not responsible for the content or functionality of any supporting materials supplied by the authors. Any queries (other than missing material) should be directed to the corresponding author for the paper.